Journal of ELECTRONIC MATERIALS, Vol. 38, No. 5, 2009
DOI: 10.1007/s11664-009-0658-x

Regular Issue Paper

The Potential of the Perturbed Angular Correlation Technique in Characterizing Semiconductors

RAKESH DOGRA,[1,5] A.P. BYRNE,[2,3] and M.C. RIDGWAY[4]

1.—Beant College of Engineering & Technology, Gurdaspur 143521, India. 2.—Department of Nuclear Physics, Research School of Physical Sciences and Engineering, Australian National University, ACT-0200 Canberra, Australia. 3.—Department of Physics, Faculty of Science, Australian National University, Canberra, Australia. 4.—Department of Electronic Materials Engineering, RSPhysSE, Australian National University, Canberra, Australia. 5.—e-mail: drdogra@yahoo.com

Several experimental techniques are available to investigate materials but microscopic techniques based on hyperfine interaction form a subclass that can characterize materials at the smallest possible atomic scale. The interaction of the nuclear electromagnetic moments with the hyperfine fields arising from the extranuclear electronic charges and spin distributions forms the basis of hyperfine methods. In this review article, one of the hyperfine methods, known as perturbed angular correlation (PAC), has been described as it provides local-scale fingerprints about the formation, identification, and lattice environment of defects and/or defect complexes in semiconductors at the PAC probe site. In particular, the potential of the PAC technique has been demonstrated in terms of measured electric field gradient, its orientation, and the symmetry at the probe site for a variety of defects in semiconductors such as Si, InP, GaAs, InAs, ZnO, GaP, and InN.

Key words: Semiconductors, perturbed angular correlation technique, implantation, defects

INTRODUCTION

Recent progress in semiconductor technology is, to some extent, due to the understanding of the nature and behavior of intrinsic and extrinsic defects in these materials, and consequently the development of techniques to control them. Defects such as vacancies, self-interstitials, antisites, dopants or impurities in semiconductors may be present as contaminants or purposely introduced, and can greatly affect the properties of semiconductors. Therefore, understanding and identifying defects in semiconductors is of scientific and technological significance. Techniques such as Rutherford backscattering/channeling spectrometry, transmission electron microscopy, double-crystal x-ray diffraction, and Raman spectroscopy have been used to reveal information about the crystal lattice of semiconductors. However, a detailed picture of the nature of defect production and their morphology is still lacking because most of the information yielded by these methods is averaged out over large length scales and they therefore lack the sensitivity to discriminate between various possible mechanisms. Information about structure on an atomic scale is possible, in principle, with techniques based on hyperfine interactions. In the following section, we discuss hyperfine interactions and one of the most suitable methods based upon them. Finally, we will emphasize the information that can be drawn from such measurements.

(Received August 28, 2008; accepted January 5, 2009; published online January 24, 2009)

Hyperfine Interactions

Hyperfine interaction studies have received distinguished recognition in solid-state material research, providing information on the local environment by observing the interaction between nuclear moments and local fields. Measurement of parameters in semiconductors such as heat capacities, electric and magnetic susceptibilities, and

neutron and x-ray diffraction represent only gross averages over the atomic-scale properties of these materials, whereas hyperfine spectroscopy probes the strength and symmetry of the local crystal fields at the microscopic scale. The basic principles of hyperfine spectroscopy[1] involve interaction of the nuclear electromagnetic moments (the electric quadrupole moment Q, and the magnetic-dipole moment μ) with the hyperfine fields (the electric field gradient EFG, and the magnetic hyperfine field MHF) arising from the extranuclear electronic charge and spin distributions in the crystal lattice. Hyperfine interaction measurements in solids directly give the corresponding electromagnetic coupling energy of the nucleus, specifically the electric quadrupole interaction and the magnetic hyperfine interaction.

A number of techniques [the Mössbauer effect (ME), nuclear orientation (NO), nuclear magnetic resonance (NMR), nuclear quadrupole resonance (NQR), electron spin resonance (ESR) and perturbed angular correlation/distribution (PAC/PAD)] have been utilized for the measurement of these hyperfine interactions.[1] These techniques partially compete with and partially complement each other. The temperature insensitivity of the PAC technique makes it better suited to follow phenomena as a function of temperature, e.g., trapping/detrapping of defects at high temperature. The PAC technique is based on the correlation between emission directions of two successive radiations emitted during a nuclear decay cascade.[1] Thus, the method requires the introduction of radioactive probe atoms into a specific site in the lattice of interest, and subsequent measurement of the emitted radiations from the atoms at these sites. For practical reasons (e.g., concerning radiochemistry, anisotropic $\gamma-\gamma$ cascade population, the half-life of the intermediate level, and the nuclear electromagnetic moments of the intermediate state), favorable PAC probes at present are very few and are summarized in Table I along with their relevant nuclear properties. A more detailed description of the PAC technique can be found elsewhere[1–4]; here we restrict ourselves to a short and relevant outline of the technique.

During PAC measurements, the radioactive probe nucleus undergoes β- or EC-decay and populates an excited level in the daughter nucleus. This excited level decays by successively emitting two γ-rays in cascade. The first γ-ray populates an intermediate isomeric level, and the second correlated γ-ray which depopulates this level due to angular momentum conservation is spatially anisotropic. After the emission of the first γ-ray, the nucleus starts to live in an intermediate state with spin direction $\vec{I}(t=0)$ and during this time the nuclear electromagnetic moments (Q or μ) interact with the hyperfine fields (MHF or EFG) at the probe nucleus. This interaction eventually causes the probe nucleus to reorient with change in the spatial

Table I. Properties of PAC Probe Nuclei

Probe	$T_{1/2}$	I	$t_{1/2}$ (ns)	$\gamma-\gamma$ (keV)	Q (b)	$\lvert\mu\rvert$ (μ_N)	$\lvert A_{22}\rvert$ (%)	Production[a]
$^{44}\mathrm{Ti} \xrightarrow{EC} {}^{44}\mathrm{Sc}$	48 y	1^-	153	78–68	0.18	0.344	4.5	$^{45}\mathrm{Sc}(p,2n)^{44}\mathrm{Ti}$
$^{77}\mathrm{Br} \xrightarrow{EC} {}^{77}\mathrm{Se}$	56 h	$5/2^-$	9.56	755–250	1.1	1.12	30	$^{75}\mathrm{As}(\alpha,2n)^{77}\mathrm{Br}$ $^{68}\mathrm{Zn}\ (^{12}\mathrm{C},xpyn)^{77}\mathrm{Br}$
$^{99}\mathrm{Mo} \xrightarrow{\beta^-} {}^{99}\mathrm{Tc}$	67 h	$5/2^+$	3.6	740–181	–	3.291	10	$^{98}\mathrm{Mo}(n,\gamma)^{99}\mathrm{Mo}$
$^{99}\mathrm{Rh} \xrightarrow{EC} {}^{99}\mathrm{Ru}$	16 d	$3/2^+$	20.5	528–90	0.23	0.284	22	$^{99}\mathrm{Ru}(d,2n)^{99}\mathrm{Rh}$
$^{100}\mathrm{Pd} \xrightarrow{EC} {}^{100}\mathrm{Rh}$	3.6 d	2^+	215	84–75	0.076	4.324	16	$^{103}\mathrm{Rh}(p,4n)^{100}\mathrm{Pd}$ $^{92}\mathrm{Zr}(^{12}\mathrm{C},4n)^{100}\mathrm{Pd}$ $^{89}\mathrm{Y}(^{16}\mathrm{O},p4n)^{100}\mathrm{Pd}$ $^{89}\mathrm{Y}(^{15}\mathrm{N},4n)^{100}\mathrm{Pd}$
$^{111}\mathrm{Ag} \xrightarrow{\beta^-} {}^{111}\mathrm{Cd}$	7.5 d	$5/2^+$	84.5	95–247	0.83	0.765	13	$^{110}\mathrm{Pd}(n,\gamma)^{111}\mathrm{Pd}$
$^{111}\mathrm{In} \xrightarrow{EC} {}^{111}\mathrm{Cd}$	2.8 d	$5/2^+$	84.5	173–247	0.83	0.765	18	$^{93}\mathrm{Nb}(^{22}\mathrm{Ne},p3n)^{111}\mathrm{In}$ $^{109}\mathrm{Ag}(\alpha,2n)^{111}\mathrm{In}$ $^{108}\mathrm{Pd}(^{6,7}\mathrm{Li},xn)^{111}\mathrm{In}$ $^{103}\mathrm{Rh}(^{12}\mathrm{C},ypxn)^{111}\mathrm{In}$
$^{111m}\mathrm{Cd} \rightarrow {}^{111}\mathrm{Cd}$	49 m	$5/2^+$	84.5	95–247	0.83	0.765	16	$^{110}\mathrm{Cd}(n,\gamma)^{111\mathrm{m}}\mathrm{Cd}$
$^{133}\mathrm{Ba} \xrightarrow{EC} {}^{133}\mathrm{Cs}$	10.5 y	$5/2^+$	6.3	356–81	0.33	3.45	3.6	$^{132}\mathrm{Ba}(n,\gamma)^{133}\mathrm{Ba}$
$^{140}\mathrm{La} \xrightarrow{\beta^-} {}^{140}\mathrm{Ce}$	40 h	4^+	3.5	329–487	0.1	4.35	13	$^{139}\mathrm{La}(n,\gamma)^{140}\mathrm{La}$
$^{172}\mathrm{Lu} \xrightarrow{EC} {}^{172}\mathrm{Yb}$	6.7 d	2^+ 3^+	1.8 8.3	1095–79 91–1095	2.16 2.87	0.67 0.65	38	$^{172}\mathrm{Yb}(p,n)^{172}\mathrm{Lu}$
$^{181}\mathrm{Hf} \xrightarrow{\beta^-} {}^{181}\mathrm{Ta}$	42 d	$5/2^+$	10.8	133–482	2.35	2.57	23	$^{180}\mathrm{Hf}(n,\gamma)^{181}\mathrm{Hf}$
$^{187}\mathrm{W} \xrightarrow{\beta^-} {}^{187}\mathrm{Re}$	24 h	$9/2^-$	554	480–134	3.3	5.11	12	$^{186}\mathrm{W}(n,\gamma)^{187}\mathrm{W}$

$T_{1/2}$, I, $t_{1/2}$, Q, μ, and A_{22}, respectively, represent the half-life of parent nuclei, intermediate spin, half-life of intermediate spin level, quadrupole moment intermediate level, magnetic moment of intermediate level, and anisotropy of the $\gamma-\gamma$ cascade under consideration; [a]Many of these radioisotopes are also available at ISOLDE@CERN, being produced in a thick target by fission, spallation or fragmentation. The singly charged ions are then accelerated to energy of 60 keV, mass separated, and then implanted into desired host.

anisotropy and to emit a second γ-ray in a direction different than if no hyperfine field is present at the probe nucleus, and the spin changes to direction $\vec{I}(t = \Delta t)$ after time Δt through an angle $\Delta\theta$. In a semiclassical picture, this effect is known as precession of the nuclear spin around the direction of the hyperfine field with precession frequency proportional to $\frac{\Delta\theta}{\Delta t}$, which results from the torque originated by hyperfine fields acting on the electromagnetic moments. In particular, this measurable effect causes a modulation of the time-dependent angular correlation pattern of the emitted γ-rays (i.e., perturbs the spatial angular correlation of the γ-rays) and forms a basis for PAC spectroscopy.

Since hyperfine fields are dominated by contributions from electronic charges and spins within the first few atomic distances around the probe atom, the more distant charges and spins only contribute to inhomogeneous broadening of signals. The precession frequencies can therefore be used to characterize the different local atomic environments around the probe atoms. Once such a frequency has been identified with an underlying environment, it can be utilized to study the following phenomena:

1. Point defects: their types, properties, interactions, radiation and implantation damage, and hydrogen trapping at defect sites
2. Surfaces and interfaces: nanostructures
3. Phase transformations: multiphase analysis, crystalline to amorphous phase transitions
4. Structural and magnetic phase transitions: critical behavior and exponents
5. Magnetism: spin dynamics, stability of atomic magnetic moments in different hosts, exchange interactions, magnetic moment formation, thin film and multilayered structures

Why Do PAC Measurements in Semiconductors?

In practice, PAC measurements are sensitive to both electric quadrupole interactions and magnetic hyperfine interactions. Electric quadrupole interactions provide a measure of the strength and symmetry of the field gradient in the vicinity of the probe nucleus. An EFG arises from the anisotropic charge distribution around the probe nucleus, and is very sensitive to the local surroundings. Therefore, the PAC technique is capable of distinguishing different lattice site locations based on their distinct and unique site-specific EFGs; for example, a cubic or tetrahedral point symmetry about a probe does not yield an EFG—a time-independent PAC spectrum is observed (Fig. 1a), whereas symmetry lowering induced by defects can lead to a unique EFG—pronounced modulations appear in the PAC spectrum and the corresponding peaks of quadrupole interaction frequency (principal component and its harmonics) appear in the Fourier spectrum as shown in Fig. 1b, the analysis of which can provide

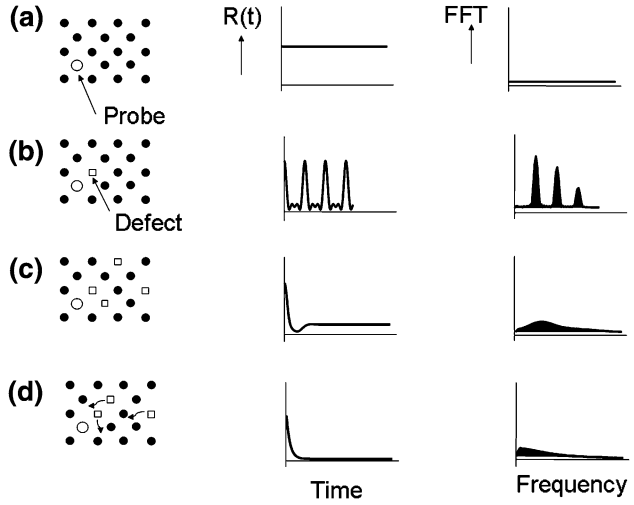

Fig. 1. Types of perturbation functions along with their respective Fourier transforms associated with different combination of EFGs. (a) zero EFG, (b) unique EFG, (c) nonunique EFG, and (d) fluctuating EFG.

information about the type of defect that produced the quadrupole interaction, i.e., the measured EFG contains information on the local symmetry and the orientation of the charge distribution with respect to the crystal axis, and delivers information on the configuration of the defect causing the EFG. If the ensemble of the probe atoms is subjected to a distribution rather than a unique EFG, the nuclear spins of the ensemble no longer display the same interaction frequency and an attenuation of the modulation amplitudes results (Fig. 1c). In this case, the perturbation function leads to finite anisotropy at large delay times. On the other hand, distribution is caused by dynamic hyperfine interactions; the anisotropy is completely destroyed, which appears as an attenuation of the angular correlation (Fig. 1d). In contrast, the magnetic hyperfine interactions, which can be measured in magnetic semiconductors (spintronics) or in the presence of external magnetic fields, are used to study the formation of magnetic moment at the probe site. Thus, semiconductors, which exhibit a variety of local environments around the probe nucleus, offer very good candidates for investigating these observations through the PAC technique.

In the past, microscopic investigations of the intrinsic (vacancies, interstitials, and antisites) and extrinsic (dopants and impurity atoms) defects in semiconductors were carried out through the determination of the defect-specific unique EFG at the probe sites by PAC spectroscopy.[5–7] In semiconductors, the possibility of pair formation is strongly enhanced if the mutual Coulombic attractions between donors and acceptors are involved. Sometimes, more complicated defect complexes consisting of more than two constituents are also formed. The formation process of these defect complexes usually

changes the electrically active impurity concentrations present in the semiconductors and hence influences the impurity diffusion. As the EFG is mainly determined by the position and the charge distribution of the atoms surrounding the probe atom, PAC spectroscopy offers a high degree of sensitivity to structural variations of the crystal lattice. This sensitivity is advantageous for discriminating the presence of intrinsic and extrinsic defects in semiconductors, which is in general a basic problem in defect studies. Extensive PAC data are available on such measurements in semiconductors,[8–25] which can be summarized as follows:

On the basis of unique and distinct EFG, indium–dopant pairs in silicon,[8–10] and indium–vacancy, indium–interstitial, and indium–carbon pairs in germanium[11,12] were identified using PAC technique with ^{111}In probe atoms. The formation of similar defect complexes was also observed in II–VI semiconductors CdTe, ZnTe, ZnSe, and $Hg_{1-x}Cd_xTe$.[13,14] The lattice site locations of implanted ^{111}In in a GaN lattice was studied by PAC spectroscopy.[15] Using ^{77}Br as probe, the metastable behavior of anion-site donors in an InAs lattice was observed[16] where the transition between the substitutional and a nonsubstitutional configuration could be detected. The presence of interstitial impurities such as transition metals, e.g., Cu in Si,[17] and hydrogen in Si[18,19] and III–V semiconductors[20] have also been identified with PAC technique. PAC technique has been successfully applied to measure the hyperfine interactions at surface sites on GaAs(111)B and InAs(111)B reconstructed surfaces using ^{111}In probe atoms.[21,22] Similar surface investigations for adsorption and desorption of Br on Si(100)-(2 × 1) surface were also performed utilizing ^{77}Br as PAC probe.[23] The successful doping of nanocrystalline ZnO with donor indium at substitutional sites has been accomplished by PAC measurements.[24] Recently, PAC spectroscopy revealed an anomalous behavior of conduction electrons at the probe site in indium-doped ZnO samples.[25] The influence of phosphorus and boron doping on the elastic properties of silicon is studied by means of the PAC method using the acceptor ^{111}In as probe[26]; a significant reduction in elastic constant of silicon with donors doping is observed, whereas acceptors did not have any influence. Apart from semiconductors, the PAC technique has also found widespread applications in other areas such as chemistry, biosciences, metals and alloys, magnetic surfaces and interfaces, etc.[27–32]

EXPERIMENTAL PROCEDURE

PAC Probe Chemistry

After receiving much recognition in nuclear physics, PAC spectroscopy has now become standard in condensed-matter physics but its utility is restricted by the fact that it involves incorporation of radioactive probe atoms in the material under investigation. In most cases, the probe atom is different from the indigenous atom and acts as an impurity in the host lattice. The chemical bonding of this impurity with the host lattice is different from in the indigenous host lattice, which leads to the so-called impurity-atom effect, giving rise to different hyperfine parameters for different probes.[4] The impurity-atom effect is manifested in the following two ways:

(i) First, it is possible that the probe atoms may occupy an isovalent site in the host lattice (e.g., ^{111}In probes in InN and InAs, and ^{111m}Cd probes in CdS and CdTe) where it decays to a donor or acceptor species prior to the γ-cascade. The hyperfine interactions take place between the excited daughter nucleus and the extranuclear fields, where the chemistry of the parent nucleus determines the site occupation in the host lattice and the properties of the daughter nucleus determine the details of hyperfine interactions. Thus, while interpreting the PAC data, the final electronic configuration of probe atoms must be considered. However, it must be kept in mind that the mobile defects in the host lattice are not trapped with the probe atom when it changes its charge state,

(ii) Second, the probe atoms, prior to decay, may itself be initially a donor or acceptor. Here, the charge difference between the probe and the indigenous ion could give rise to the probe trapping various point defects (e.g., ^{111}In probes as acceptor in doped n-Si, forming donor–acceptor pairs). This effect depends upon the concentration of the probe ions as well as its crystal symmetry. Depending upon the mobility of these defects, the defects may remain trapped with the probe ions even after the probes undergo decay. Thus, the trapping or detrapping of various point defects is governed by the parent nucleus whereas the measured EFG at the daughter nucleus gives information about the electronic structure of the defect complex with the daughter nucleus.

The above discussion makes it evident that the availability of appropriate probe atoms plays a very decisive role in PAC measurements. One major problem is that of sample preparation, in which probe atoms must be introduced without changing the properties of the host materials. PAC experiments can be performed with radioactive probe atoms at concentrations much lower than 1 ppm. (Note that for such a low concentration of probe atoms, the impurity–impurity interactions are negligibly small.) To dope a material with the requisite radioisotope probe, the following procedures can be used:

1. Thermal treatment of the sample, so that the probe atoms are introduced via diffusion or melting[33]

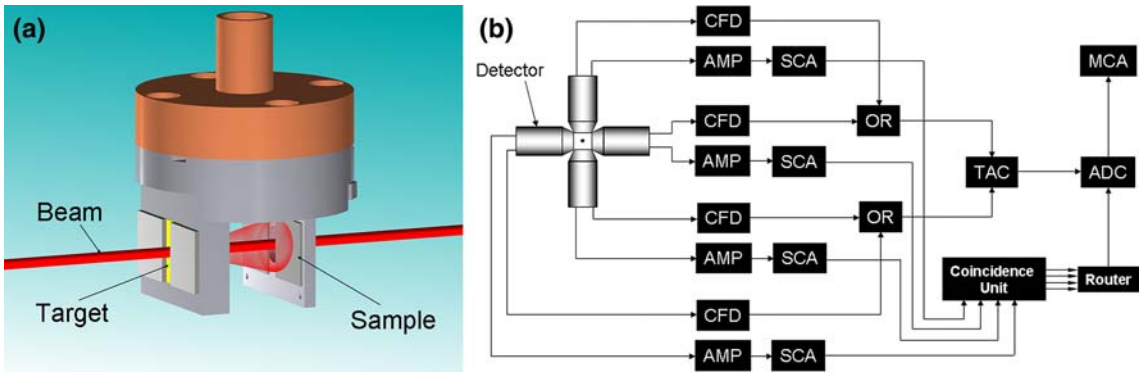

Fig. 2. (a) Experimental setup for production and recoil implantation of PAC probes following heavy ion reactions. (b) A typical PAC setup comprises four scintillator detectors (BaF_2/NaI(Tl)). This 90 deg to 180 deg detector geometry is used if the two γ-rays are detected along either the ⟨100⟩ or ⟨110⟩ lattice directions. If the γ-rays are detected along ⟨111⟩ lattice directions, the detectors have to be replaced by 70.9 deg to 109.1 deg. The electronic modules SCA, AMP, CFD, OR, ADC, TAC, and MCA, respectively represent the single channel analyser, spectroscopic amplifier, constant fraction discriminator, or-gate, analog to digital converter, time to amplitude converter, and multichannel analyser.

2. Through chemical reaction, i.e., *in situ* preparation of sample with radioisotope probe[34]
3. Implantation and/or recoil implantation of radioactive ions into the sample[35]

Thermal treatment of the samples leads to a well-defined metallurgical state of the impurity in the respective semiconductor and is not suitable for semiconductors having low vapor pressure, e.g., Se, Te, and their compounds. The chemical reaction method is well suited to polycrystalline materials which can be prepared through chemical reaction (citrate gel process, coprecipitation, and complex compound process) and during sample preparation the required quantity of radioactive probe can be added. The radioactive material is homogeneously distributed in the sample and this homogeneity is usually retained even after sintering at high temperature. The advantage of the third procedure (i.e., implantation) is its applicability to all isotopes, even in the case of probe atoms with low solubility in the host, e.g., rare-earths in silicon, materials that are difficult to fabricate (complex or pure), and layered structures. With the help of sufficiently high implantation energies, the problem of diffusion barriers such as oxide layers at the surface can be overcome. The tracers are almost carrier-free (i.e., do not contain significant amount of stable isotopes of same element), and thus studies of systems with low solid solubility are possible. Probes such as $^{111}In \rightarrow {}^{111}Cd$, the most commonly used PAC probe, can be prepared carrier-free and thus about 10^{11} to 10^{12} radioactive atoms are sufficient in the sample to perform PAC studies. Such low probe concentrations eventually do not affect the macroscopic structure and properties of the material under investigation. On the other hand, probes such as $^{181}Hf \rightarrow {}^{181}Ta$ (produced by irradiating stable Hf isotopes with thermal neutrons) cannot be prepared carrier-free and generally contain a very small proportion of radioactive atoms along with a significant amount of stable isotopes. Thus, such probes are usually produced with a very high specific activity so that only a small amount of probe atoms needs to be added to the sample under study.

For the PAC measurements described in this review, we utilized the recoil implantation method using the ANU Pelletron accelerator, for which a special chamber was designed (Fig. 2a). This method has the advantage of *in situ* production of the radioisotope and immediate implantation into the desired host lattice. We made use of the following nuclear reactions to produce radioactive probe atoms that subsequently recoil-implant the probe atoms into the desired hosts:

$$^{103}Rh(^{12}C, xpyn)\{^{111}Sn, ^{111}Sb\} \rightarrow {}^{111}In \text{ with } {}^{12}C \text{ beam energy of } 70\,MeV$$

$$^{92}Zr(^{12}C, 4n)^{100}Pd \text{ with } {}^{12}C \text{ beam energy of } 70\,MeV$$

The momentum transferred to the reaction products leads to recoil implantation into the desired host. The samples were positioned behind the target foil and away from the transmitted projectile beam axis, subtending scattering angles of ~2 deg to 300 deg. As the angular distribution of recoiled probe atoms is broader than that of scattered projectile beam, this allows efficient collection of probe atoms without significant projectile contamination. Generally, implanted activity of the order of 1 μCi to 2 μCi is sufficient to carry out PAC measurements. The other radioisotopes produced by competing nuclear reactions do not disturb the PAC measurements, as these are either short-lived species that decay rapidly, or their reaction cross sections are very low.

PAC Setup and Data Acquisition

A typical PAC setup is shown in Fig. 2b,[1] where the sample containing the radioactive probe atoms is placed at the center of the detector assembly.

The γ-rays, which proceed and follow the long-lived intermediate state, are detected by scintillation detectors coupled to photomultiplier tubes. PAC setups usually employ BaF_2 scintillator detectors, which have superior time resolution compared with NaI(Tl) scintillator or Ge detectors.[36] Cerium-doped $LaBr_3$ scintillators* have shown excellent energy resolution for γ-ray detection in comparison with NaI(Tl) scintillator, higher efficiency due to higher Z-content and better time resolution in comparison with BaF_2 scintillators.[37] Recently, PAC measurements using $LaBr_3$(Ce) scintillator detectors have been performed with ^{44}Ti probe atoms, where the γ–γ cascade of 68 keV to 78 keV could easily be resolved.[38] The times of the start and stop signals are determined by constant fraction discriminators (CFD) before being fed to a time-to-amplitude (TAC) counter. The multichannel analyzer records the time intervals between the start and stop γ-rays. The recorded time distribution is a lifetime decay curve modulated by the spin precessions of the nucleus by hyperfine fields. Analysis of time distribution curves provides information about the hyperfine fields present in the sample. To keep the sample at the desired temperature, a specially designed tubular furnace of diameter about 3 cm to 4 cm can be installed at the center of the detector's geometry. Recently, a new-generation fully digital PAC spectrometer has been designed and built,[39] which is capable of performing software-based data processing with all the benefits of storage, repeatable data analysis under different limits, and easy switching between different isotopes.

PAC Measurements and Analysis

Experimentally, the primary quantity measured in a PAC experiment is the coincident time distribution[1–3] $W(\theta,t)$ of γ-rays in the γ–γ cascade populating and depopulating the intermediate level. This can be obtained by recording the coincidence counting rate when the succeeding γ-ray is detected at time t after the first γ-ray detection at an angle θ. The coincidences are generally recorded at the desired temperatures using a standard setup of detectors arranged in planar 90 deg to 180 deg geometry.

For polycrystalline samples, the time distribution function $W(\theta,t)$ can be written as an expansion of the Legendre polynomial $P_k(\cos\theta)$,

$$W(\theta,t) = \exp(-t/\tau_N)\left[1 + A_{22}G_{22}(t)P_2(\cos\theta) + A_{44}G_{44}(t)P_4(\cos\theta)\right], \quad (1)$$

where time-independent terms A_{kk} (k = 2, 4) denote the anisotropy coefficients which contain the spatial correlation information of the γ–γ cascade involved. The time-dependent functions $G_{22}(t)$ and $G_{44}(t)$ depend on the nature of the hyperfine fields and contain all the desired information about the hyperfine interaction of the probe ion with its environment. In most cases $A_{44} \ll A_{22}$, and hence the higher-order terms in the above expression are often neglected. The numerical reduction of these distributions removes the effects of exponential decay and provides an experimental quantity known as the ratio function or perturbation function, $R(t)$, which shows the effects of modulation and is given by[1]

$$R(t) = 2\frac{[C(180\,\text{deg},t) - C(90\,\text{deg},t)]}{[C(180\,\text{deg},t) - 2C(90\,\text{deg},t)]},$$

where $C(\theta,t)$ is the geometric mean of the coincidences taken from the spectra recorded at angles 180 deg and 90 deg, respectively. The detailed data reduction methodology for PAC measurements using different detector setups is given in Arends et al.[40]

In the paramagnetic phase of the material, the measured perturbation function $R(t)$ is fitted with a suitable model for the static nuclear electric quadrupole interaction:

$$R(t) = A_{22}G_{22}(t) = A_{22}\sum_i f_i G_{22}^i(t) + C. \quad (2)$$

Here, f_i are the fractional site populations and C is the time-independent baseline shift that takes into account the effects of γ-rays that are absorbed by the sample en route to the detectors and the effects of probe atoms that are not in well-defined chemical environments. $G_{22}^i(t)$ are the corresponding perturbation factors given by

$$G_{22}^i(t) = \sum_n s_{2n_i}(\theta_j,\eta_i)\cos(\omega_{n_i}(\eta_i)t) \times \exp\left(\frac{-(\delta_i\omega_{n_i}t)^p}{p}\right).\exp\left(\frac{-(\tau_R\omega_{n_i}t)^2}{2}\right), \quad (3)$$

where the transition frequencies ω_n and their amplitudes S_{2n} are related to the hyperfine splitting of the intermediate nuclear level and are determined by diagonalization of the interaction Hamiltonian. The term ω_n depends on the nuclear quadrupole frequency ω_Q ($\omega_n = 6\omega_Q$ for a half-integer spin and $\omega_n = 3\omega_Q$ for an integer spin) and the EFG tensor V_{ij} ($i, j = x, y, z$), where EFG is defined as the second spatial derivative of the electric potential V at the nuclear site. In the principal axis system of the EFG tensor, where only the diagonal components are nonzero and $V_{xx} + V_{yy} + V_{zz} = 0$, the EFG is usually expressed in terms of the largest component V_{zz}. The nonvanishing component of the EFG V_{zz} is related to the quadrupole frequency ω_Q by $\omega_Q = eQV_{zz}/4I(2I-1)\hbar$ and is measured in terms of the spin-independent quadrupole

*$LaBr_3$(Ce), NaI(Tl), and BaF_2 scintillator detectors, respectively have energy resolution of 3%, 7% to 8%, and 11% to 13% at 662 keV γ-ray, whereas their respective time resolution using 511 keV annihilation γ-rays is 260 ps, 500 ps, and 1000 ps.

frequency $\nu_Q = eQV_{zz}/h$, where Q is the nuclear electric quadrupole moment. The quadrupole frequency, ν_Q, is known as the coupling constant and contains information about the strength of the interaction. The deviation of the EFG from axial symmetry is given by the asymmetry parameter $\eta = (V_{xx} - V_{yy})/V_{zz}$ with $0 \leq \eta \leq 1$. For $\eta = 0$, the perturbation function is harmonic and periodic, but for a nonzero value of η, the oscillations in the perturbation function are periodic and nonharmonic. The detector system should have sufficient time resolution in order to distinguish the different contributions towards the observed perturbation function. The effects of the finite time resolution, τ_R, of detectors and the distribution of EFG with width δ ($p = 1$ and $p = 2$ represent Lorentzian and Gaussian type distributions, respectively) are properly taken into account in Eq. 3. If the measurement is carried out on a single crystal, it is possible to extract the orientation of V_{zz} relative to the crystal axes from the Euler angles, θ_j, contained in the $S_{2n}(\theta_j,\eta_i)$ coefficients.

RESULTS AND DISCUSSIONS

In the following section, we discuss some of the important information that can be obtained from PAC measurements in semiconductors:

Local Structure around Probes: Site Allocations

Since the perturbation function $R(t)$ is characteristic of the particular surroundings of the probe nucleus, if chemically different surroundings are present in a particular system, then the measured perturbation function will reflect the abundance of each contribution. Analysis of the observed perturbation function can make it possible to separate these different contributions in the system and thus assign these contributions to specific positions in the system. An example of this is illustrated in Fig. 3. The perturbation function along with its Fourier transform for InAs observed with an $^{111}In/^{111}Cd$ probe is shown in Fig. 3a; the time-independent perturbation function clearly indicates the cubic symmetry of the probe atoms in the crystal lattice. In contrast, the defect-induced symmetry lowering in highly doped Si leads to a modulation pattern in the PAC spectra (Fig. 3b, c), as observed with $^{100}Pd/Rh$ probe atoms.[41,42] The least-squares fit of the PAC data gave interaction frequencies of 13.1(2) MHz and 35.5(4) MHz, respectively, in highly doped n- and p-Si corresponding to symmetric EFG oriented along ⟨111⟩ direction. These results revealed the formation of Pd–V and Pd–B defect complexes, respectively, in highly doped n- and p-Si. Figure 3d shows the PAC spectrum of polycrystalline synthesized InN, where the least-squares fitted parameters reveal the presence of In_2O_3 contents in the sample;[43] the starting materials for synthesis was In_2O_3. Besides, we observed

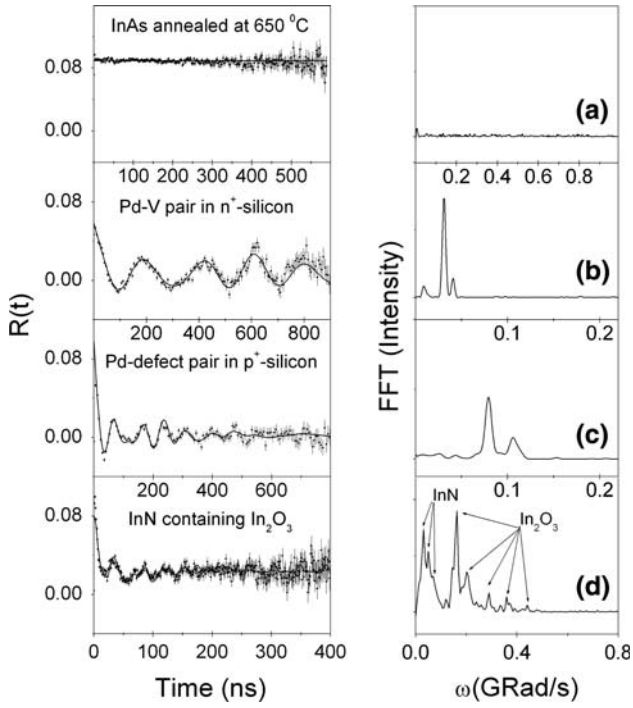

Fig. 3. Least-squares-fitted PAC spectra and their respective Fourier transforms. (a) time-independent spectrum showing cubic symmetry about probe nucleus ($^{111}In/Cd$) in InAs, (b) and (c) showing defects trapped at probe site ($^{100}Pd/Rh$) in highly doped silicon, and (d) showing presence of contaminated phase in InN using $^{111}In/Cd$ probe nucleus.

an interaction frequency of 28 MHz having a broad distribution with a small nonzero value of asymmetry parameter at the indium site in an InN crystal lattice. The small but nonzero value of asymmetry parameter in the InN lattice indicates the broken symmetry around the cation ion, whereas the broad distribution in the measured EFG at the cation site suggests that defects are inherent to the lattice of InN.

EFG and Their Distributions

In a defect-free crystal, where each probe nucleus in the crystal lattice interacts with an identical EFG, the measurement of the static probe site EFG should yield well-defined interaction frequencies, i.e., δ should be very small. Figure 4d shows the PAC spectrum for a single crystal of n-ZnO annealed at 1273 K in ambient nitrogen after recoil-implanting $^{111}In/Cd$ probe atoms; the sharp lines in the Fourier spectrum reveal the presence of a single EFG. On the other hand, the measurements yield a broad distribution (i.e., large δ) when small intrinsic defects (such as point defects, disordered structure or impurities) lie in the neighborhood of the probe ion, since each probe atoms in the lattice interacts with a somewhat different EFG. Therefore, this large distribution in EFGs will cause a damping of the amplitudes of the PAC pattern with increasing time. Figure 4a shows the PAC spectrum for as-implanted ZnO where damping of the spectrum

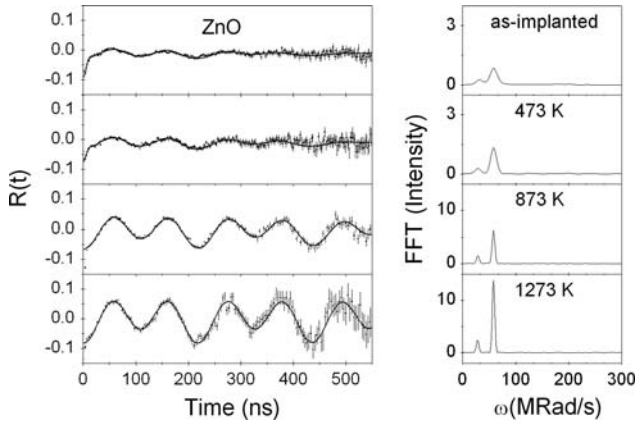

Fig. 4. PAC time spectra as a function of annealing temperature in a single crystal of *n*-ZnO acquired with ^{111}In/Cd probe. Solid lines are the least-squares fit of the appropriate theoretical function to the experimental data.

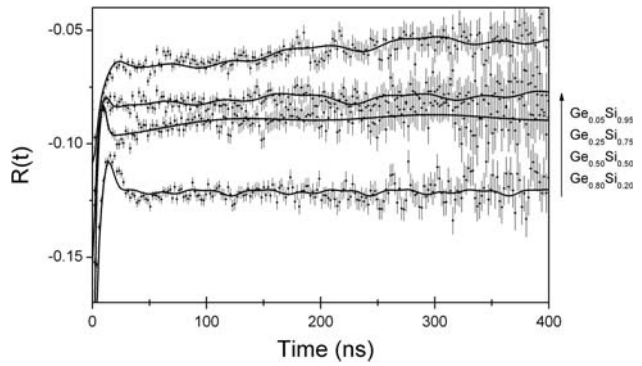

Fig. 5. Perturbation functions for ^{111}In/Cd probes in Ge_xSi_{1-x} semiconductor alloys at room temperature. Solid lines are the least-squares fit of the appropriate theoretical function to the experimental data. The damped spectra indicate that not all probe atoms are observing the same EFG.

is caused by radiation damage. The high-purity ZnO single crystal was recoil-implanted with ^{111}In probe atoms following nuclear reactions. Recoils with energy of up to 8 MeV produce sufficient damage in the host lattice, which is observed as attenuation in the PAC spectrum. We also performed PAC measurements in substitutionally disordered Ge_xSi_{1-x} alloy following recoil implantation of ^{111}In/Cd probe atoms. The measured room-temperature perturbation functions are shown in Fig. 5 for samples annealed in flowing nitrogen at 923 K for 30 min. The observed damping in the PAC spectra is inherent, due to local randomness in the alloy. In view of the large number of possible microscopic Si–Ge combinations, one should expect a broad distribution in the PAC pattern of electric quadrupole interaction, leading to strong damping. Note that the PAC spectra for pure Si and Ge are time independent because of cubic symmetry about the probe. Thus, the PAC measurements in defect-free semiconductors will yield site-specific EFGs, whereas in disordered semiconductors or semiconductors with distant defects, they will give distributed EFGs that may mask the actual values.

Dopant-Defect/Dopant Interaction

Since PAC measurements usually involve impurity atoms, which generally differ in size or charge from the atoms of the host material, the measured hyperfine parameters may differ from the ones measured using an identical probe–host atom combination. That is why Mössbauer and PAC measurements give quite different results for the same material studied. At the same time, these size and charge differences can be important when the PAC technique is applied to characterize point defects in the materials, as probe atoms can trap vacancies and interstitials. The presence of these point defects in the neighborhood of the probe breaks the local point symmetry of the crystal lattice, which in turn generates an EFG at the probe site and this EFG differs in magnitude and symmetry from the probe site EFG generated by a perfect crystal lattice. Analysis of the isochronal annealing dependence of the hyperfine parameters can provide useful information concerning the trapping of defects, their diffusion, formation energies, etc. Moreover, the EFG sensed by PAC probe atoms represent the local point symmetry about the probe and not necessarily the overall symmetry of the crystal. In the past, PAC spectroscopy has been utilized to observe the dopant-defect/dopant interaction in various semiconductors, e.g., using ^{111}In/Cd probe atoms, In-defect/dopant pairs have been observed in Ge[11,12] and Si.[8–10,17–19,44]

Recently, we have observed such pairs with ^{100}Pd/Rh probe atoms in highly doped Si, i.e., Pd–vacancy defect pair in highly doped *n*-Si[41] and Pd–B defect pair in highly doped *p*-Si.[42] The corresponding PAC spectra are shown in Fig. 3b and c. The Pd–V pair was observed for as-implanted samples, and maximum population was observed after an annealing between 473 K and 573 K for 30 min in ambient nitrogen. The Pd–B defect pair was observed only for the annealed sample and the maximum population was attained at an annealing temperature of around 888 K.

EFG Orientation

PAC measurements are also helpful to deduce the orientation of the EFG relative to the crystal lattice and hence the local structure of probe atoms. Three measurements are generally carried out, with the sample mounted between the detectors in such a way that either ⟨100⟩ and ⟨110⟩, or ⟨111⟩ axes of the crystal are pointing towards the detectors. Here, we illustrate this for Pd–V pair in silicon (Fig. 6). Visual inspection of the spectra clearly shows the differences. A comparison to theoretically calculated patterns for the principal component of the EFG oriented along each of these main directions

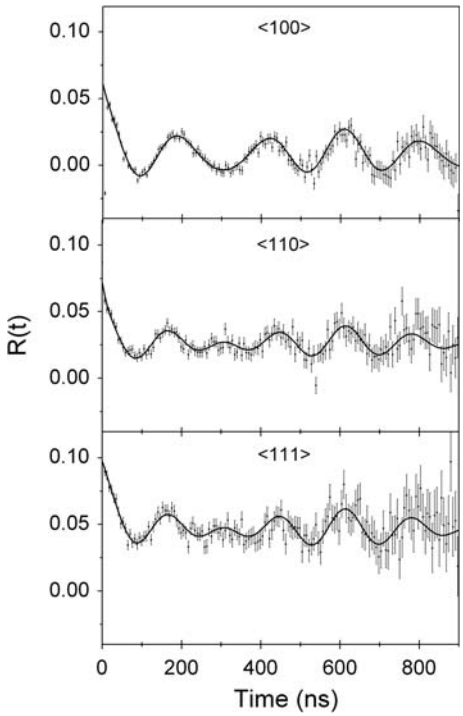

Fig. 6. Time-dependent anisotropy observed for ^{100}Pd/Rh probe in highly doped *n*-type silicon sample for different orientations relative to the detectors. The sample was annealed at 523 K for 30 min and measured at room temperature. Solid lines are the least-squares fit of the appropriate theoretical function to the experimental data.

unambiguously yields a ⟨111⟩ orientation of EFG. The observed symmetric EFG oriented along the ⟨111⟩ direction is compatible with the structure of a dumbbell consisting of a substitutional palladium probe and silicon vacancy on a nearest-neighbor lattice site.

Isochronal Annealing

Radiation Damage Annealing

Microscopic techniques such as PAC are capable of studying the impurity–defect interaction. When impurity atoms are implanted in the host matrix, this produces radiation damage and the position of the impurity and distribution of defects created by implantation are correlated. Information on the formation and dissociation of impurity–defect complexes can be obtained during an annealing process by measuring the EFG caused by the defects in the immediate vicinity of the probe. Such an effect has been observed for an *n*-ZnO single crystal following recoil implantation of the probe atoms ^{111}In. Figure 4 shows the PAC spectrum of *n*-ZnO measured at room temperature following recoil implantation of probe atoms and after various isochronal annealing sequences. The successive annealing steps lead to a reduction of radiation damage caused during recoil implantation; the corresponding increase in amplitude of the modulations can be seen. After annealing of radiation

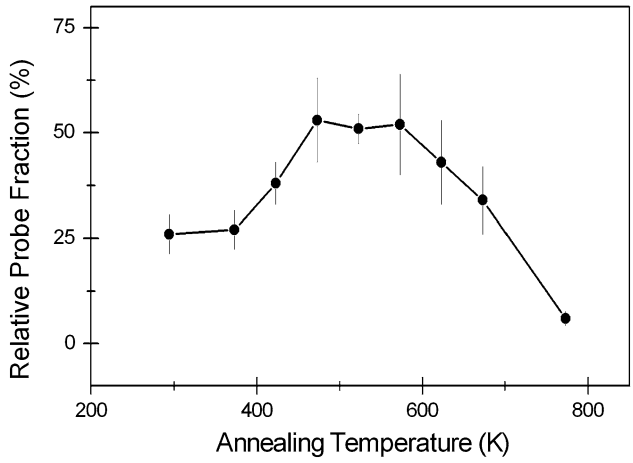

Fig. 7. Relative probe function as a function of annealing temperature in highly doped *n*-Si with ^{100}Pd/Rh probe atoms. The line is a guide to the eye.

damage at 1,273 K we observed an axially symmetric EFG oriented along [0001] characterized by the quadrupole interaction frequency 30.6(3) MHz. The observed EFG is attributed to substitutional incorporation of probe atoms at zinc sites.[45] Similar results have also been observed in a single crystal of GaP[46] using the PAC technique with radioisotope probe atoms ^{111}In/Cd.

Thermal Stability of Defects

Isochronal annealing can also be utilized to study the thermal stability of the defect complexes in semiconductors. Such measurements were performed for the Pd–V and Pd–B defect complexes in silicon.[41,42] Figure 7 shows the fractional population of Pd–V defect complex as a function of annealing temperature. The Pd–V pair shows a maximum population at an annealing temperature of around 473 K to 573 K and starts dissociating at around 773 K. Using first-order kinetics, the activation energy for the dissociation of the defect complex is estimated to be 2.5(7) eV. Similar behavior was also observed for Pd–B defect pair with activation energy for dissociation estimated to be 2.3(8) eV; the defect pair was found to be stable between annealing temperatures of 823 K and 1023 K.

Temperature Dependence of EFG

PAC spectroscopy also allows us to determine the temperature dependence of the average EFG. This additional information is of interest because the temperature dependence is governed by the vibration of constituents in the vicinity of the probe atoms. The temperature dependence of the quadrupole interaction frequency (and hence EFG) for the Pd–V pair was performed between 77 K and 703 K.[42] As the sample temperature increased, the quadrupole interaction frequency of the complex decreased monotonically, as shown in Fig. 8, which could be least-squares fitted according to the relation

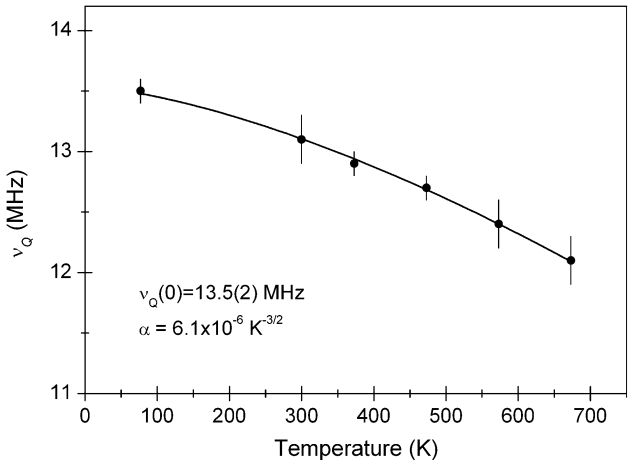

Fig. 8. Temperature dependence of measured quadrupole interaction frequency, ν_Q, in highly doped *n*-type silicon with ^{100}Pd/Rh probe. The solid lines in the figure represent a least-squares fit of the function $\nu_Q(T) = \nu_Q(0)\left[1 - \alpha T^{3/2}\right]$ to the data points.

$\nu_Q(T) = \nu_Q(0)\left[1 - \alpha T^{3/2}\right]$. The coefficient $\left[1 - \alpha T^{3/2}\right]$ is intended to take into account the effect caused by thermal lattice expansion and vibration. However, in semiconductors, thermal effects alone are not sufficient to explain such a strong variation of quadrupole interaction frequency with temperature. The different charge states of the defect complex might be responsible as the Fermi level shifts towards mid gap with increasing temperature, which eventually changes the ionization probability of the defect complexes.

Crystalline to Amorphous Phase Transitions

The PAC technique can be used to follow changes at a microscopic scale when new micro-surroundings at the probe site start appearing, such as change of bond distances, change of symmetry, trapping of defects, etc., causing changes in the EFG value. An example of a phase transition mechanism studied by the PAC technique in III–V group compound semiconductor as a function of implanted ion-dose is shown in Fig. 9a. These measurements yielded information about the cubic to disordered to amorphous phase transition. The extracted amorphous fraction as a function of ion dose is plotted in Fig. 9b and an appropriate amorphization model can be quantified from the same. Using PAC spectroscopy a direct amorphization process consistent with the *overlap model* in InP,[47] a direct amorphization process, and growth of amorphous zones due to defect stimulation in GaAs and accumulation of simple point defects and then direct-impact/defect-stimulated mechanism for InAs have been identified.[48]

Structural Relaxation of Amorphous Phase

The structural relaxation effects resulting from room-temperature annealing in amorphous

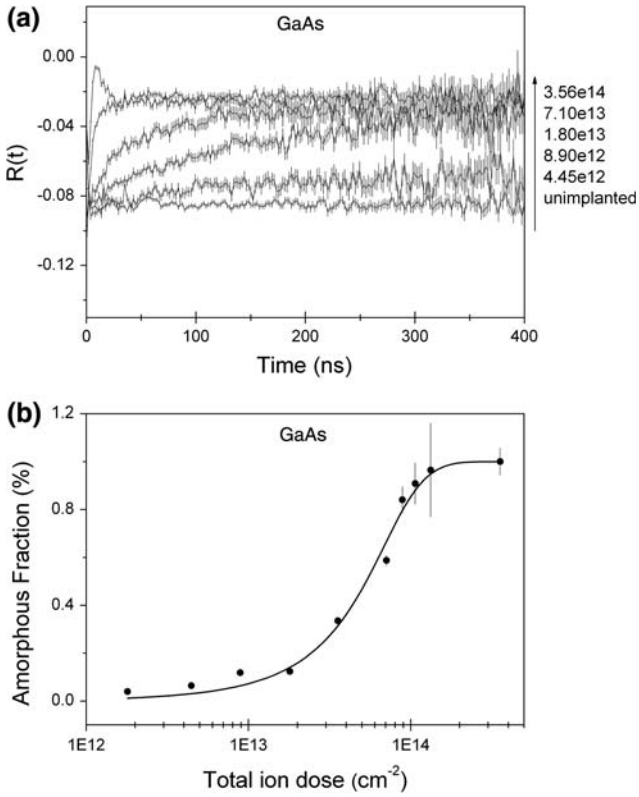

Fig. 9. (a) Least-squares-fitted PAC spectra measured at room temperature for GaAs using ^{111}In/Cd probe implanted at indicated Ge ion doses. Samples were implanted at liquid-nitrogen temperature. (b) Amorphous fraction deduced from PAC spectra as a function of total Ge ion dose. The curve represents the crystalline to amorphous phase transition. The solid line corresponds to the least-squares fit to a model that represents a direct amorphization process and growth of amorphous zones due to defect stimulation.

semiconductors can also be studied by PAC spectroscopy. The transition from as-implanted state to thermally annealed state is irreversible and is known to occur due to recovery of topological short-range order in the network and/or annihilation of point defects. From the measured PAC spectra, which were acquired as a function of room-temperature annealing time in ion-implanted InP, the fraction of probes in an amorphous environment is extracted and shown in Fig. 10. The amorphous zones in InP were produced by MeV Ge ion implantation at liquid-nitrogen temperature. The observed behavior could be fitted with the exponential decay function comprising two characteristic relaxation times: a fast initial recovery time τ_1 and a slower recovery time τ_2.[49] In contrast, no room-temperature annealing time dependence was observed for samples irradiated with an ion dose greater than that required for amorphization or equivalently; the fraction of radioactive probes in an amorphous environment remained constant at a value of one (100%). This indicates that amorphous zones of larger size possess larger activation energies for thermal annealing.

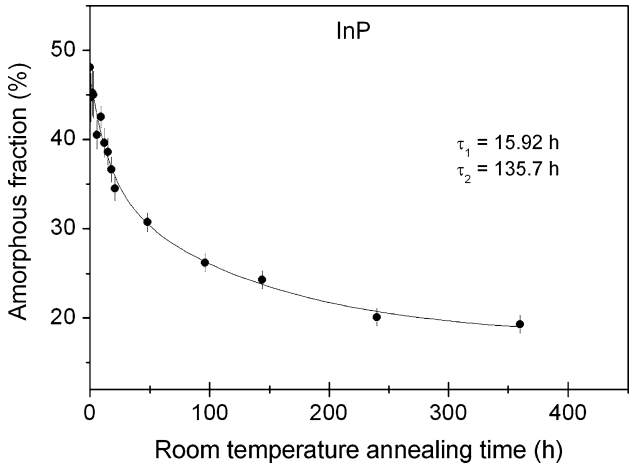

Fig. 10. Amorphous fraction for InP deduced from PAC measurements as a function of room-temperature annealing time. Amorphous zones were produced at liquid-nitrogen temperature by implanting MeV Ge ions.

CONCLUSIONS

To perform all these PAC measurements in elemental and compound semiconductors, we developed an installation at the ANU heavy-ion facility for production and subsequent recoil implantation of an appropriate probe into the crystal lattice of interest. The potential of PAC spectroscopy can be exploited to obtain a variety of atomic-scale information in semiconductors. This review illustrates examples of: (a) lattice site location of implanted impurities on the basis of strength, symmetry, and orientation of EFG; (b) EFGs and their distribution caused by defects in the immediate vicinity of impurity atoms; (c) dopant-defect/dopant interactions and their thermal stability, which is useful to deduce the dissociation energy of the defect complex; (d) investigation of the annealing of radiation damage caused by implanted impurities (these studies will be beneficial in order to know the annealing temperature at which crystallinity will recover); (e) investigation of the Fermi level effect by performing temperature dependence of EFG; (f) crystalline–amorphous phase transitions on application of ion implantation; and (g) room-temperature relaxation of the amorphous phase produced by ion implantation.

ACKNOWLEDGEMENTS

The authors acknowledge the academic and accelerator staff of the ANU heavy-ion facility for their assistance in this work. We also thank Genevieve Hussain for careful reading of the manuscript and valuable suggestions.

REFERENCES

1. G. Schatz and A. Weidinger, *Nuclear Condensed Matter Physics: Nuclear Methods and Applications*, 2nd ed. (New York: Wiley, 1996).
2. H. Frauenfelder and R.M. Steffen, *Alpha, Beta and Gamma Ray Spectroscopy*, ed. K. Siegbahn (Amsterdam: North Holland, 1965), p. 997.
3. T. Wichert and E. Recknagel, *Microscopic Methods in Metals*, ed. U. Gonser (Berlin: Springer, 1986), p. 317.
4. G.L. Catchen, *MRS Bull.* 20, 37 (1995).
5. Th. Wichert, *Identification of Defects in Semiconductors. Semiconductors and Semimetals*, Vol. 51B, ed. M. Stavola (London: Academic Press, 1998/1999), p. 297.
6. Thomas Wichert and Manfred Deicher, *Nucl. Phys. A* 693, 327 (2001). doi:10.1016/S0375-9474(00)00688-6.
7. M. Deicher, *Hyp. Int.* 79, 681 (1993). doi:10.1007/BF00567596.
8. Th. Wichert and M.L. Swanson, *J. Appl. Phys.* 66, 3026 (1989). doi:10.1063/1.344188.
9. Th. Wichert, M.L. Swanson, and A.F. Quenneville, *Phys. Rev. Lett.* 57, 1757 (1986). doi:10.1103/PhysRevLett.57.1757.
10. G. Tessema and R. Vianden, *Appl. Phys. A* 81, 1471 (2005). doi:10.1007/s00339-005-3249-6.
11. H. Haesslein, R. Sielemann, and Ch. Zistl, *Phys. Rev. Lett.* 80, 2626 (1998). doi:10.1103/PhysRevLett.80.2626.
12. G. Tessema and R. Vianden, *J. Phys. Condens. Matter* 15, 5297 (2003). doi:10.1088/0953-8984/15/30/311.
13. V. Ostheimer, S. Lany, J. Hamann, H. Wolf, Th. Wichert, and ISOLDE Collaboration, *Phys. Rev. B* 68, 235206 (2003). doi:10.1103/PhysRevB.68.235206.
14. J.C. Austin, Wm.C. Hughes, B.K. Patnaik, R. Triboulet, and M.L. Swanson, *J. Appl. Phys.* 86, 3576 (1999). doi:10.1063/1.371261.
15. K. Lorenz, F. Ruske, and R. Vianden, *Appl. Phys. Lett.* 80, 4531 (2002). doi:10.1063/1.1485117.
16. M. Risse and R. Vianden, *J. Appl. Phys.* 93, 2648 (2003). doi:10.1063/1.1539288.
17. R. Keller, M. Deicher, W. Pfeiffer, H. Skudlik, D. Steiner, and Th. Wichert, *Phys. Rev. Lett.* 65, 2023 (1990). doi:10.1103/PhysRevLett.65.2023.
18. H. Skudlik, M. Deicher, R. Keller, R. Magerle, W. Pfeiffer, P. Pross, E. Recknagel, and Th. Wichert, *Phys. Rev. B* 46, 2159 (1992). doi:10.1103/PhysRevB.46.2159.
19. M. Gebhard, B. Vogt, and W. Witthuhn, *Phys. Rev. Lett.* 67, 847 (1991). doi:10.1103/PhysRevLett.67.847.
20. M. Deicher and W. Pfeiffer, *Hydrogen in Compound Semiconductors*, ed. S.J. Pearton (Material Science Forum 148–149, Trans Tech Publications, 1994), p. 481.
21. J.M. Adam, G.L. Catchen, J. Fu, and D.L. Miller, *Surf. Sci.* 337, 118 (1995). doi:10.1016/0039-6028(95)00532-3.
22. G.L. Catchen, D. Loubychev, and R. Platzer, *Hyp. Int.* 136/137, 633 (2001). doi:10.1023/A:1020586808228.
23. J. Lohmuller, H.H. Bertschat, H. Granzer, H. Haas, G. Schatz, and W.-D. ZeitzISOLDE Collaboration, *Surf. Sci.* 360, 213 (1996). doi:10.1016/0039-6028(96)00682-6.
24. Th. Agne, Z. Guan, X.M. Li, H. Wolf, Th. Wichert, H. Natter, and R. Hempelmann, *Appl. Phys. Lett.* 83, 1204 (2003). doi:10.1063/1.1598289.
25. W. Sato, Y. Itsuki, S. Morimoto, H. Susuki, S. Nasu, A. Shinohara, and Y. Ohkubo, *Phys. Rev. B* 78, 045319 (2008). doi:10.1103/PhysRevB.78.045319.
26. N. Santen and R. Vianden, *Mater. Sci. Eng. B* 154–155, 126 (2008).
27. L. Hemmingsen and T. Butz, *Application of Physical Methods to Inorganic and Bioinorganic Chemistry. Encyclopedia of Inorganic Chemistry Books*, ed. R.A. Scott (2007).
28. Y. Ohkubo, Y. Murakami, W. Sato, and A. Yokoyama, *J. Nucl. Radiochem. Sci.* 8, 79 (2007).
29. S. Zhu, Y. Zheng, Y. Zuo, D. Zhou, D. Yuan, A. Li, Z. Wang, X. Duan, M. Liu, and Y. Li, *J. Radioanal. Nucl. Chem.* 272, 615 (2007). doi:10.1007/s10967-007-0634-y.
30. G.S. Collins, S.L. Shropshire, and J. Fan, *Hyp. Int.* 62, 1 (1990). doi:10.1007/BF02407659.
31. H.H. Bertschat, K. Potzger, A. Weber, and W.-D. Zeitz, *Eur. Phys. J. A* 13, 233 (2002).
32. L.G. Shpinkova, A.A. Sorokin, B.A. Komissarova, G.K. Ryasnyi, V.N. Kulakov, and S.M. Nikitin, *Meas. Tech.* 42, 490 (1999). doi:10.1007/BF02504474.

33. A.W. Carbonari, J. Mestnik, R.N. Saxena, R. Dogra, and J.A.H. Coaquira, *Hyp. Int.* 136, 345 (2001). doi:10.1023/A:1020533708556.
34. R. Dogra, A.C. Junqueira, R.N. Saxena, A.W. Carbonari J. Mestnik-Filho, and M. Moralles, *Phys. Rev. B* 63, 224104 (2001). doi:10.1103/PhysRevB.63.224104.
35. H.E. Mahnke, *Nucl. Phys. A* 588, 221c (1995). doi:10.1016/0375-9474(95)00143-O.
36. A. Baudry, P. Boyer, and P. Vulliet, *Hyp. Int.* 13, 263 (1983). doi:10.1007/BF01027256.
37. M. Balcerzyk, M. Moszynski, and M. Kapusta, *Nucl. Inst. Methods A* 537, 50 (2005). doi:10.1016/j.nima.2004.07.233.
38. S.-b. Ryu, S.K. Das, and T. Butz, *Phys. Rev. B* 77, 094124 (2008). doi:10.1103/PhysRevB.77.094124.
39. C. Herden, J. Röder, J.A. Gardner, and K.D. Becker, *Nucl. Inst. Methods A* 594, 155 (2008). doi:10.1016/j.nima.2008.05.001.
40. A.R. Arends, C. Hohenemser, F. Pleiter, H. de Waard L. Chow, and R.M. Suter, *Hyp. Int.* 8, 191 (1980). doi:10.1007/BF01026869.
41. D.A. Brett, R. Dogra, A.P. Byrne, J. Mestnik-Filho, and M.C. Ridgway, *Phys. Rev. B* 72, 193202 (2005). doi:10.1103/PhysRevB.72.193202.
42. R. Dogra, D.A. Brett, A.P. Byrne, and M.C. Ridgway, *Hyp. Int.* 33, 177 (2007).
43. R. Dogra, S.K. Shrestha, A.P. Byrne, M.C. Ridgway, A.V.J. Edge, R. Vianden, J. Penner, and H. Timmers, *J. Phys. Condens. Matter* 17, 6037 (2005).
44. N. Achtziger, S. Deubler, D. Forkel, H. Wolf, and W. Witthuhn, *Appl. Phys. Lett.* 55, 766 (1989). doi:10.1063/1.102265.
45. R. Dogra, A.P. Byrne, and M.C. Ridgway, *Opt. Mater.* (2009) (accepted).
46. R. Dogra, Z.S. Hussain, and A.K. Sharma, *Mater. Charact.* 58, 652 (2007). doi:10.1016/j.matchar.2006.07.014.
47. E. Bezakova, A.P. Byrne, C.J. Glover, M.C. Ridgway, and R. Vianden, *Appl. Phys. Lett.* 75, 1923 (1999). doi:10.1063/1.124872.
48. R. Dogra, A.P. Byrne, Z.S. Hussain, and M.C. Ridgway, *Nucl. Instr. Methods B* 266, 1460 (2008). doi:10.1016/j.nimb.2007.11.058.
49. R. Dogra, A.P. Byrne, L.L. Araujo, and M.C. Ridgway, *Nucl. Instr. Methods B* 257, 355 (2007). doi:10.1016/j.nimb.2007.01.137.